AIAA JOURNAL
Vol. 46, No. 5, May 2008

Three-Dimensional Unsteady Flow Computations Around a Conventional Slat of High-Lift Devices

Taro Imamura,* Shunji Enomoto,† Yuzuru Yokokawa,* and Kazuomi Yamamoto‡
Japan Aerospace Exploration Agency (JAXA), Chofu, Tokyo 182-8522, Japan

DOI: 10.2514/1.25660

Three-dimensional unsteady flow structure inside a deployed slat of high-lift configuration is simulated numerically to investigate the cause of slat noise. Because the Reynolds number of the flow is high and the geometry is complex, a zonal large eddy simulation/Reynolds-averaged Navier–Stokes hybrid method is used to reduce the overall computational cost. The power spectral density of the pressure coefficient is compared to the experiment, and some issues regarding grid resolution, order of numerical scheme, and number of subiterations for implicit time integration are discussed. Two different types of fluctuations (high-frequency narrowband and low-frequency broadband) are observed, and the computational results are consistent with the experiment. Careful observation of the unsteady computational data reveals longitudinal vortical structures under the lower surface of the slat, which is consistent with the previous studies. The low-frequency broadband fluctuation becomes large around this region. Therefore, it is assumed that these longitudinal vortical structures are causing the broadband noise from the slat.

Nomenclature

C_p	=	pressure coefficient
C_s	=	Smagorinsky constant
c	=	stowed wing chord
c_{slat}	=	slat chord
d	=	distance from the wall
F_{switch}	=	switching function for defining LES/RANS regions
q	=	Powell noise source
Re	=	Reynolds number
u_i	=	velocity components of the instantaneous flow
$\bar{u}_i$	=	time-averaged velocity components
u'_i	=	velocity fluctuating components of the instantaneous flow
x, y, z	=	coordinates in streamwise, vertical, spanwise direction
α	=	filter constant
Δt	=	time step
Δx	=	grid size
Δy^+	=	the grid size for the first row of the cell off the wall in wall units
ν_T	=	eddy viscosity
ρ_0	=	mean flow density
$\boldsymbol{\omega}$	=	vorticity vector

I. Introduction

DURING the landing phase, the noise from high-lift devices (HLD) is an important contributor to the overall noise from the airframe [1], and the reduction of this type of noise is one of the key technologies for future aircraft development. There are strong demands in noise prediction and reduction technologies. The aerodynamic coefficients of HLD are sensitive to its geometry as well as setting and improving aerodynamic performance of HLD has a strong impact on the operating cost. Therefore, simply installing noise reduction devices to HLD will end up with weight penalty, as well as decrease in aerodynamic performance. To design low-noise HLD without decreasing aerodynamics performance, it is important to understand the flow physics around HLD from both aerodynamics and aeroacoustics points of view.

In this study, we focus on the leading-edge slat of HLD. Many studies based on experiment [2–5] and computation [6–11] have been performed. From the previous studies, two different types of noise have been observed around slat. The first component, high-frequency narrowband noise, is caused by the trailing-edge thickness of slat. The dominant frequency is consistent with the vortex shedding frequency from the trailing edge. The second component is a low-frequency broadband component. Although this component has been observed in experiments, the noise generation mechanism is not clearly understood.

Regarding computation studies, most of previous studies have been based on 2-D Reynolds-averaged Navier–Stokes (RANS) computations. Khorrami et al. [8] have performed 2-D RANS and unsteady RANS calculations and have compared the velocity field with particle image velocimetry (PIV) data. Although good agreement was obtained for mean flow properties, they reported that there are significant differences in unsteady vortical structures inside the slat cove. Recently, 3-D computations around different slat configurations have been reported by several authors [9–11]. Terracol et al. [9] have performed a zonal RANS/LES (large eddy simulation) and observed important differences concerning the mean flowfield in the slat cove between steady computation and zonal RANS/LES. They have computed power spectral density (PSD) of pressure fluctuation inside the slat cove focusing on the high-frequency narrowband peak caused by the slat trailing edge. Deck [10] has performed a zonal detached eddy simulation (DES) and compared the velocity profile inside the coves of slat and main element. Velocity profile around the slat has been compared to PIV measurement data, which was obtained from the EUROPIV2 project. The compared mean velocity and root-mean square of the velocity fluctuation was consistent with the experiment. Choudhari et al. [11] have performed a zonal Laminar/RANS hybrid simulation. They have compared mean flow properties and turbulent kinetic energy (TKE) distribution with previous PIV measurements performed at NASA Langley and observed the importance of 3-D computation. Although most of the studies focus on flowfield structure, which has a strong relation with noise source structures, it is not clear how accurately unsteady simulations are predicting the unsteady fluctuations because comparisons

Presented as Paper 2668 at the 12th AIAA/CEAS Aeroacoustics Conference, Hyatt Regency Cambridge, Cambridge, Massachusetts, 8–10 May 2006; received 6 June 2006; revision received 10 May 2007; accepted for publication 12 May 2007.

*Researcher, Aviation Program Group, 7-44-1 Jindaiji-Higashi. Member AIAA.
†Manager, Aviation Program Group, 7-44-1 Jindaiji-Higashi. Member AIAA.
‡Manager, Aviation Program Group, 7-44-1 Jindaiji-Higashi. Senior Member AIAA.

with experiments for unsteady components are limited to the root-mean square of velocity fluctuation and TKE in previous researches. For the purpose of noise prediction, comparison of pressure fluctuation spectra between experiments is necessary to assess numerical data.

Based on the preceding discussions, 3-D unsteady computational in the slat cove of HLD is performed using a zonal-LES/RANS hybrid code (UPACS-LES code [12–14]). This paper focuses on understanding the near fieldflow structure inside the slat cove. High-order schemes are used to solve convective terms with a filtering method. The computed results are assessed by changing the grid resolution, order of numerical scheme, and number of subiterations for implicit time integration. By comparing the PSD of unsteady pressure fluctuation with experimental data, the current status of unsteady simulation for predicting unsteady components are investigated.

This paper is organized as follows. Section II briefly describes the computational model for HLD, numerical methods, and the setup used in this study. Section III presents the computational results. The computed steady and unsteady components are presented. Especially, the unsteady components are compared with the experiment changing grid resolution, order of numerical scheme, and number of subiterations for implicit time integration. Based on the computational data, the flowfield inside the slat cove region is observed in detail. Finally, Sec. IV concludes this paper.

II. Numerical Setup

A. Computational Model for High-Lift Devices

Figure 1 shows a model for a wind-tunnel testing which was conducted from 2005 to 2006 at the low-speed wind tunnel (JAXA-LWT1), which is a closed-circuit wind tunnel with a 6.5×5.5 m cross section [15,16]. The test is carried out to provide experimental data for computational fluid dynamics (CFD) validation and to know flow physics for a realistic aircraft takeoff and landing configuration deploying HLD. That is a semispan model which is 2.3 m in spanwise width. For the approach configuration of interest in the present study, the setting of HLD at the reference cross section is as follows. The slat gap is 0.5%, the flap gap is 1.0%, and the slat and flap overlap settings equal 1.7% and 1.7%, respectively. Also, the deflection angles of the slat and flap are 25 and 35 deg, respectively. The model is assuming a 100 passenger class civil transport, which has a nacelle-pylon, leading-edge slat, inner double-slotted fowler flap, and outer single-slotted fowler flap with flap-track fairing (FTF). The slat and flap settings are for the landing condition. Based on this configuration, we chose a cross section of the wing located at 1.44 m from the wing root in Fig. 1b where unsteady pressure transducers are installed. The chord length at this cross section is 0.426 m under stowed configuration. A 3-D computational model is made without a sweep angle and taper to analyze noise generation mechanism around the slat more simply. The width in the spanwise direction is defined based on the previous studies. Terracol et al. [9] have performed computations varying the computational domain width (2.7 and 27% slat chord length) in spanwise direction. They reported that the spanwise unstable mode is not large enough for a 2.7% c_{slat} case. Deck [10] and Choudhari et al. [11] have used grids which have 25 and 37.3% c_{slat} in the spanwise direction, respectively. Thus, we extended the grid in the spanwise direction up to 34.1% c_{slat}. The mean flow Mach number is 0.2 and the angle of attack is 4 deg based on the approach condition. The Reynolds number, based on the chord length of the stowed wing and the mean flow velocity is 1.8×10^6.

B. Definition of the LES/RANS Region and Computational Grids

In this study, we focus on the unsteadiness of the flow in the slat cove. To reduce the computational cost, the slat region is computed by LES [17] and the rest of the region is calculated by the Spalart–Allmaras (SA) one-equation model [18]. The switching between LES and RANS (SA) is performed by a switching function F_{switch},

$$F_{\text{switch}} = \begin{cases} 1 & x/c \le 0.15 \cdots \text{LES} \\ 0 & 0.25 \le x/c \cdots \text{RANS(SA)} \\ -10(x/c) + 2.5 & 0.15 \le x/c \le 0.25 \cdots \text{transient region} \end{cases} \tag{1}$$

and is described in Fig. 2. Because the formulations of LES and RANS are similar, the switching of each zone can be performed by using the following equation:

$$\nu_T = F_{\text{switch}}(\text{SGS model}) + (1 - F_{\text{switch}})(\text{eddy viscosity of RANS}) \tag{2}$$

Several other switching functions were tested before this choice. We found that this switching function is simple as well as the best for the purpose of suppressing the reflection wave at the boundary of the LES and RANS regions so far.

For wall bounded flows, the amount of cells N needed for a LES computation scales as $N \sim Re^{1.8}$, giving a number of cells of the order of 10^9, which is too large to be solved. Although the minimum grid size is sufficiently small ($\Delta y^+ < 1$ around the lower surface of the slat), rapid extension of the grid off the surface of the wall is necessary to suppress the number of overall grid points. In other words, it is assumed that a sufficient number of cells could not be located inside the boundary layer of the LES region. Consequently, the boundary layer turbulence is not resolved in the current computations. However, considering that the purpose of this study is to gain further information related with the noise source around slat, resolving the boundary layer accurately around the slat is not so important. From the previous studies [9–11], it is estimated that the important part of this problem is unsteadiness from the slat cusp, not the boundary layer. To investigate whether this assumption is reasonable, PSD of C_p will be compared with the experimental results.

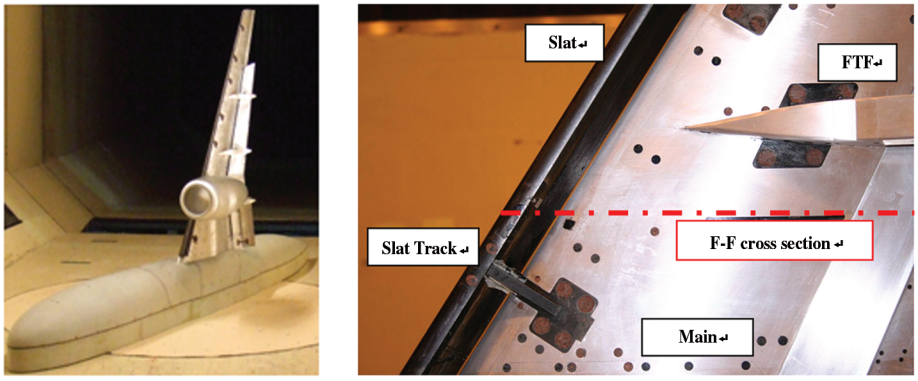

a) Overall view b) Closeup view around the slat cove from the lower side

Fig. 1 JAXA high-lift device wind-tunnel testing model.

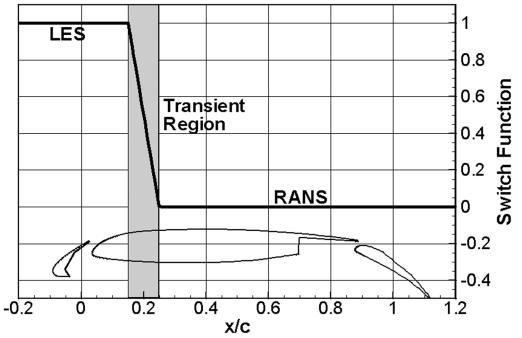

Fig. 2 Switching of LES/RANS region by the switching function.

Based on the preceding discussions, the grid sizes in each direction inside the slat cove region should be almost uniform (excluding the boundary layer) to allow the complicated vortical flow structures to evolve. Two grids are generated by changing the resolution. Figure 3a describes the chordwise cross-sectional 2-D grid distribution, and Fig. 3b shows the close-up view around the slat cove region. The grid points are packed into the slat cove region to resolve unsteady vortical structure. Nearly 20% of the total grid points are located in the slat cove. The grid sizes inside the slat cove (excluding near the wall) for coarse and fine grids are 0.68 and 0.34% of the slat chord, respectively. Consequently, the total grid points turn out to be the numbers listed in Table 1. The grid size in the spanwise direction is uniform.

The treatment of the slat wake region is also important because if the grid stretches rapidly, reflection waves will be observed when vortices pass by. Therefore, the grid width in the flow direction gradually increases at the wake of the slat trailing edge to gradually smooth out the vortices.

C. CFD Solver and Numerical Conditions

Numerical methods used in the calculation are briefly described. In this study, we use a flow solver called UPACS-LES [12–14]. This flow solver is developed based on the UPACS code. The governing equations are the compressible Navier–Stokes equations.

$$\frac{\partial \mathbf{Q}}{\partial t} + \frac{\partial \mathbf{F}_j}{\partial x_j} + \frac{\partial \mathbf{F}_{Vj}}{\partial x_j} = 0 \tag{3}$$

where

$$\mathbf{Q} = \begin{pmatrix} \rho \\ \rho u_i \\ E \end{pmatrix}, \qquad \mathbf{F}_j = \begin{pmatrix} \rho u_j \\ \rho u_j u_i + p\delta_{ij} \\ \rho u_j H \end{pmatrix},$$
$$\mathbf{F}_{Vj} = \begin{pmatrix} 0 \\ -\tau_{ij} \\ -\tau_{ij} u_i - \kappa \frac{\partial T}{\partial x_j} \end{pmatrix} \tag{4}$$

The standard Smagorinsky model [17] with $C_s = 0.1$ is used for the LES computation, and the Spalart–Allmaras one-equation model [18] is used for the RANS computation. As for the subgrid scale (SGS) modeling, the dynamic Smagorinsky model or the implicit LES are often used recently. However, the dependency of the results to the choice of the SGS model is still an unresolved issue. As for the definition of C_s, it is decided that there are no firm methods to define the value for this kind of complex flow. The classification of a flow as an external or internal flow has an impact on the choice of C_s ($C_s = 0.1$ and 0.2 for internal and external, respectively). Overall, it is an external flow, but focusing around the slot region between the slat and the main element, it could be realized as an internal flow. Therefore, $C_s = 0.1$ is chosen in this study.

The flow solver of the current version is based on a cell-centered finite-volume method on multiblock structured grids. The code is parallelized by a flexible domain decomposition concept and Message-Passing Interface (MPI). The simulations are performed using characteristic boundary conditions along the far-field boundaries in the chordwise cross-sectional plane, except for extrapolation from the interior at the downstream boundary. The periodic boundary condition is applied to the spanwise direction and no-slip boundary conditions are imposed at the solid surfaces. At the wall boundary of the LES region, van Driest damping is applied.

Zonal-LES/RANS simulations are performed in the following procedures. First, RANS (SA) computations are performed to obtain a steady-state flowfield as an initial condition for the unsteady computations. The initial conditions for RANS computations are the mean flow. Second, zonal-LES/RANS computations are performed to obtain unsteady flow. The simulations are run over a long duration that consisted of at least 11.6 to 21.3 slat flow-through time units to minimize the transient effects. No acceleration is added to enforce the unsteadiness of the flow. And finally, unsteady computations are performed to obtain the flow statistics. To reduce the convergence error in the flow statistics, the simulations are run over 11.6 slat flow-through time units.

As discussed earlier, the computational grid is coarser than the ideal grid for LES. Thus, grid dependency has to be checked. Also, it is recognized that the order of the scheme has an influence on the results. Numerical accuracy due to the number of subiterations for implicit time integration is also an open issue for unsteady computations. Therefore, the computed results are assessed by

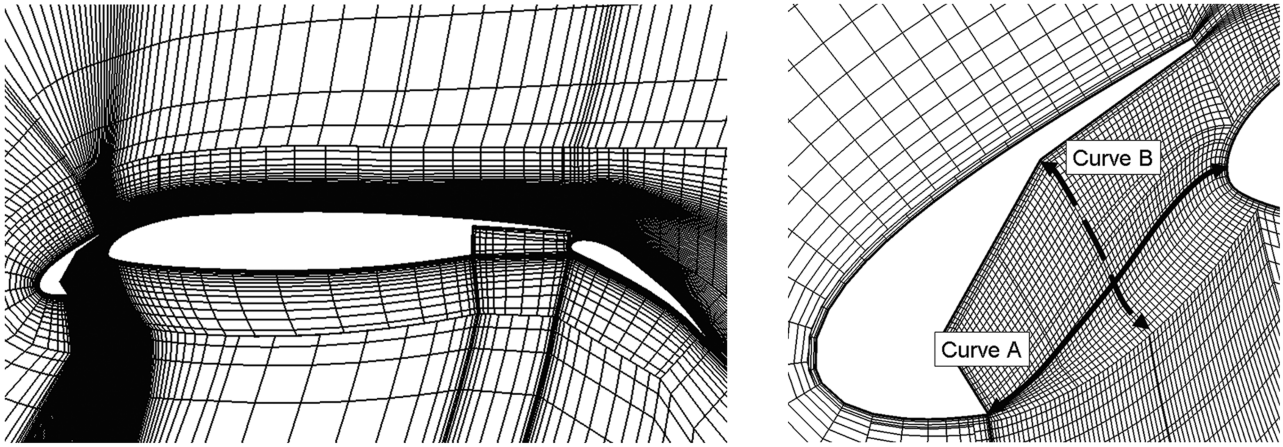

a) Chordwise cross sectional 2D grid distribution **b) Close-up view around slat cove region**

Fig. 3 Computational grid (2-D cross section). Every four points are drawn for the fine grid.

Table 1 Grid details

	Coarse grid	Fine grid
Total grid points	1.91 million	13.45 million
Blocks	74	79
Grid points along curve A[a]	162	320
Grid points along curve B[a]	66	131
Grid points at slat trailing edge	25	25
Spanwise grid points	33	65

[a]Curves A and B are shown in Fig. 3b.

changing the grid resolution, order of numerical scheme, and number of subiterations for implicit time integration. The details of the computations are summarized in Table 2. Cases 1 and 2 are steady-state RANS computations on coarse and fine grids, respectively. Convection terms are discretized using the Roe scheme with third-order Monotone Upstream-Centered Schemes for Conservation Laws (MUSCL) and no limiter is imposed. First order time integration is performed by an implicit method using the matrix–free Gauss–Seidel (MFGS) scheme [19] with a local time stepping technique. The Courant–Friedrichs–Levy (CFL) number, defined as

$$\mathrm{CFL} = \frac{U\Delta t}{\Delta x} \tag{5}$$

where U is the characteristic velocity, is set to 100. Computations are performed until the convergence is achieved. The fluctuation of the density is monitored and the computation is performed until this value becomes lower than 10^{-10} per point. Because the aim of the computations is not focused on the prediction of drag, this criterion is found out to be sufficient.

Cases 3 (coarse grid), and 4 to 6 (fine grid) are zonal-LES/RANS hybrid computations. For cases 3, 5, and 6, high-order schemes are used. The convection terms are discretized using the sixth-order compact scheme developed by Kobayashi [20]. The viscous terms are discretized using the second-order central scheme. The reason for using different orders for different terms is only due to the numerical stability. It is better to discredit the diffusion term by the sixth-order scheme, as well as the convection term. Concerning the overall accuracy, it should be defined by the truncation error term of the lowest term. Therefore, in overall, it is second order. However, because the Reynolds number is high, the effect of the viscous term is small. In other words, the order of the convection term seems to dominate the overall accuracy. We think this is the reason why we have observed differences when different schemes (third order and sixth order) are used for the convection term as shown later. At the boundary (including the interface of the block) the fourth-order scheme is used. Also, the compact scheme is used in both the LES and RANS region. To avoid numerical instability, the sixth-order filter developed by Gaitonde and Visbal [21] is used. Several values for filter constants are tested before the computations. Considering the stability and the accuracy, filter constant [22] α is defined as 0.45 in this study. The convection term for case 4 is discretized using the Roe scheme with third-order MUSCL and no limiter imposed. Second-order time integration is performed by MFGS [19] with three (cases 3 to 5) and five (case 6) subiterations. The nondimensional time steps using the chord length of the stowed wing and sonic speed as reference values are set to $\Delta t = 4\mathrm{e}-4$ and $2\mathrm{e}-4$ for coarse and fine grids, respectively. These values are chosen to satisfy the CFL condition (CFL < 1) in the slat cove, excluding the boundary layer. This constraint must be satisfied to prevent the numerical dissipation of the acoustic waves and vorticity inside the LES regions.

III. Computational Results

First of all, we will start by validating the numerical results. Both time-averaged and unsteady components are assessed through the comparisons between different computational cases and experimental results. Especially, the effects of grid resolution, order of numerical scheme, and number of subiterations for implicit time integration to PSD of C_p are examined. Finally, using the computational data, detail flow structures inside the slat cove are examined.

A. Time-Averaged Flowfield

We will start by looking at the time-averaged flowfield. For zonal-LES/RANS results, the data are averaged in the time over the last 20,000 and 40,000 steps for coarse and fine grids, respectively.

Figure 4 shows the time-averaged streamlines around the slat cove region for case 5. There is a large recirculating region in the slat cove region, and it is bounded by a shear layer generated from the slat cusp. The shear layer impinges the lower surface of the slat. On the upper surface, no separation is observed. Table 3 summarizes the location of the center of the recirculation zone and reattachment point. In the study by Terracol et al. [9], they have observed obvious differences between steady-state RANS and time-averaged RANS/LES hybrid methods results in the mean flow pattern. But in the current geometry, the differences in the location of the center of the recirculation zone and the reattachment point among the computed cases are less than 0.03 c_{slat}, and the difference in the flow pattern is not observed.

Figure 5 shows the comparison of C_p distributions around the HLD. The results of cases 1, 2, 3, and 5 are shown here to see the effect of the turbulence modeling and the effect of the grid resolutions. For case 3, LES treatment around the slat region and the use of the low-resolution grid lead to lower negative pressure over the slat upper surface. Because of the incorrect prediction around the slat region, the distribution on the main and flap also becomes different from the other results. Excluding case 3, the C_p distribution on the slat, main, and flap surfaces shows good agreement with each other. At this flow condition, suction peak does not appear near the leading edge of the slat.

Figure 6 compares streamwise velocity components along the line, which passes though the center of the recirculation zone as described in the same figure. The locations of the center of the recirculation zone, where u/U_∞ becomes 0.0, are consistent for all cases. Once again, for case 3, the LES treatment around the slat region and the use of the low-resolution grid lead to the over estimations of the local maximum streamwise velocity at $d/c = 0.05$ compared with the rest of the results. Excluding case 3, the rest of the results are consistent with each other. To predict the mean flow properties with the zonal-LES/RANS hybrid method, a fine grid is required for the current case.

B. Validation of Computed Results (Power Spectral Density)

The PSD of C_p is calculated at the unsteady pressure measurement locations to compare with the experimental results. The locations of the unsteady pressure measurements are shown in Fig. 7a. Points A and B are located on the slat cove. Point C is

Table 2 Computations performed in this study

	Mode	Grid	Scheme	Subiterations
Case 1	RANS	Coarse	Roe third	——
Case 2	RANS	Fine	Roe third	——
Case 3	Zonal-LES/RANS	Coarse	Compact sixth	3
Case 4	Zonal-LES/RANS	Fine	Roe third	3
Case 5	Zonal-LES/RANS	Fine	Compact sixth	3
Case 6	Zonal-LES/RANS	Fine	Compact sixth	5

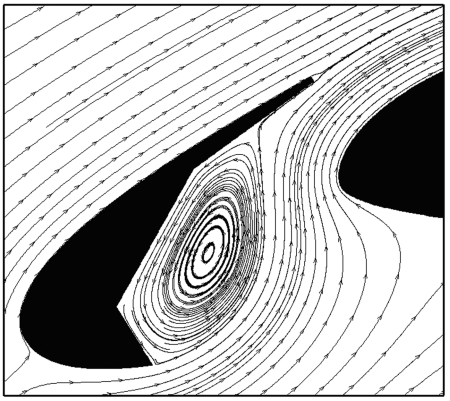

Fig. 4 Time-averaged streamlines in the slat cove region (case 5).

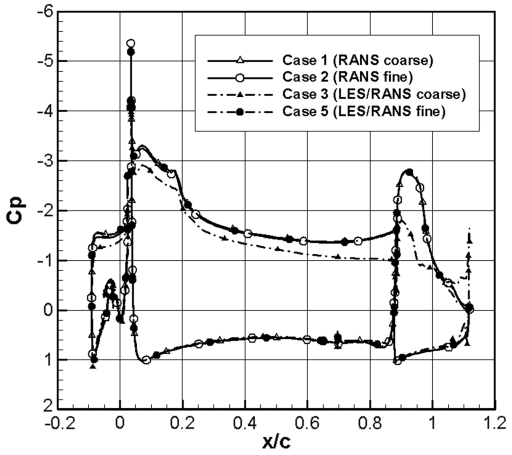

Fig. 5 Comparison of the pressure coefficient distribution around the airfoil.

located on the leading edge of the main element. The numerical results are compared with the unsteady pressure measurement data. In the experiment, KULITE transducers (XCS-062) are used with A/D sampling frequency of 80 kHz. The pressure transducers on the slat (points A and B) are mounted parallel to the wall with the cavity. At point C, on the leading edge of the main element, the pressure receiver is flush mounted to the surface. To calibrate the transducers, the calibration data provided by the KULITE is used. The obtained data are averaged over 400 spectra to reduce the convergence error of flow statistics and the reproducibility of the PSD distribution is verified.

There are several differences between the experiment and the numerical simulations that might lead to differences in the PSD distributions. First of all, there are obvious geometrical differences between the wind tunnel and the computational models, although the cross-sectional geometry is the same. The wind-tunnel model is a fully 3-D configuration with a sweep angle of 33 deg, taper, FTF, slat track, and a dihedral angle of 3 deg, etc. During this experiment, the slat boundary layer is not tripped. On the other hand, the computational model does not have the preceding listed items. Among these items, the sweep angle might have an effect on the PSD of C_p, but the influences of other items are expected to be small. For example, the effect of the taper is expected to be small because the computation is performed on a limited spanwise extent (5% difference in spanwise direction corresponds to $0.012c$ differences in the chordwise length). Also, the effects from FTF and the slat tracks are expected to be small because there is some distance from the measuring points (see Fig. 1a). Second, flow conditions are slightly different. As for the experiment, the mean flow velocity is 70 m/s and the angle of attack is 3.5 deg, whereas those for the computations are 69.2 m/s and 4.0 deg, respectively. Considering these differences, qualitative comparisons are made hereafter.

For the purpose of reducing the convergence error in the flow statistics, the computations should be performed over a long duration. Computing such long duration is very time consuming and only averaging over eight spectral with a Hanning window before frequency analysis is available in the current study. Therefore, averaging in the spanwise direction will also be performed after the PSD calculation of a single point. As a result, the C_p data are averaged over 128 (16 points in the spanwise direction) and 256 (32 points in the spanwise direction) spectra for the coarse and fine grids, respectively. The sensitivity of the convergence error to the number of averaging is checked and the current averaging number seems to be sufficient.

Table 3 Location of the center of the recirculation zone and reattachment

	Center of the recirculation zone	Reattachment
Case 1	(−0.018, −0.031)	(0.002, 0.021)
Case 2	(−0.016, −0.030)	(0.003, 0.021)
Case 3	(−0.017, −0.030)	(0.005, 0.022)
Case 4	(−0.017, −0.027)	(0.004, 0.022)
Case 5	(−0.014, −0.030)	(0.001, 0.020)
Case 6	(−0.015, −0.027)	(0.003, 0.022)

First, we will check the result of case 5. The PSD of C_p at points A, B, and C are compared with the experimental data as shown in Figs. 7b–7d. At the high-frequency region (around 20 kHz), a peak is observed at all points. This frequency is consistent with the vortex shedding from the slat trailing edge. At point A, the level and frequency of the high-frequency narrowband peak are consistent with the experiment, but at points B and C, the peak levels are under- and overestimated, respectively. On the other hand, at the low-frequency region (lower than 10 kHz), broadband characteristics can be observed from the PSD at all points. At points A and C, good agreements are observed concerning the level and the distribution of the low-frequency broadband component. At point B, the level of the broadband component is lower than the experiment. It is difficult to locate the causes of these differences from the available data. However, considering the geometrical difference discussed earlier, the overall agreement is relatively good.

Next, the effects of the grid resolution, order of numerical scheme, and number of subiterations for time integration are examined. Among the current computational cases, case 3 shows relatively good agreement with the experiment. However, we think of this agreement as just a coincidence because the difference is observed in the mean flow properties (see Fig. 5). For case 4, the results are similar to that of case 5, except for the differences around 5 to 15 kHz. The reason for this discrepancy will be discussed in the following section. For case 6, the overall tendency is almost the same with that of case 5. By increasing the number of subiterations, slight

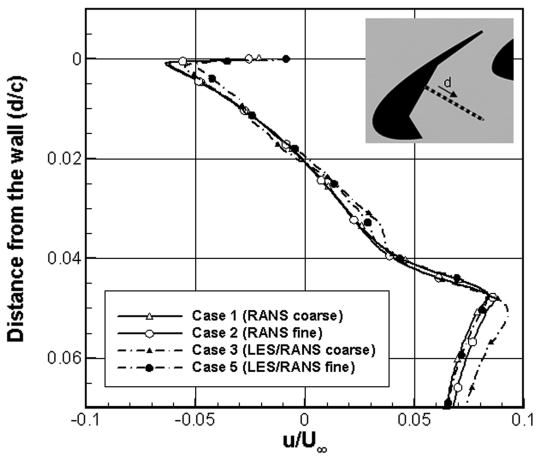

Fig. 6 Comparison of the streamwise velocity component along the line shown in the figure.

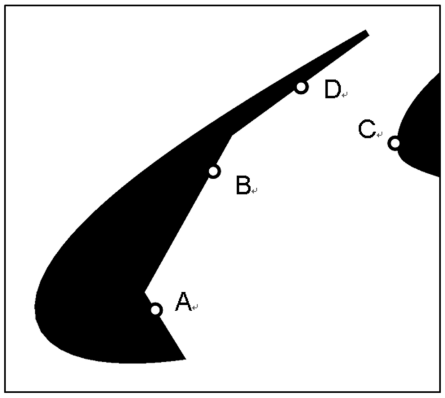

a) Unsteady pressure measurement locations

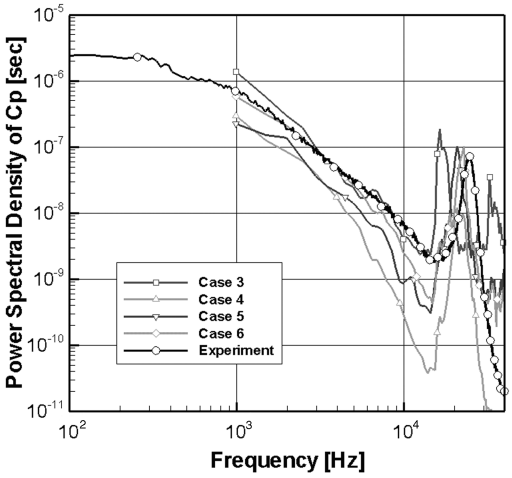

b) PSD at Point A

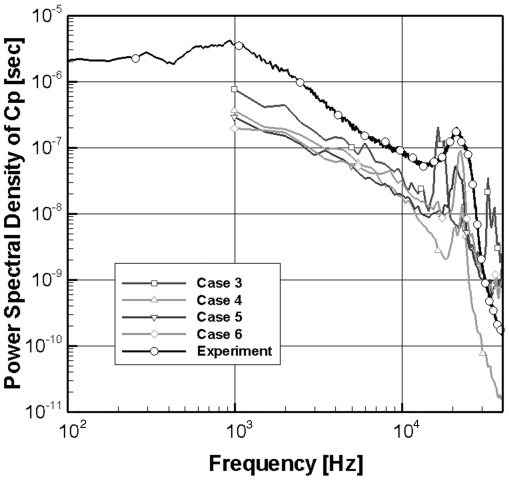

c) PSD at Point B

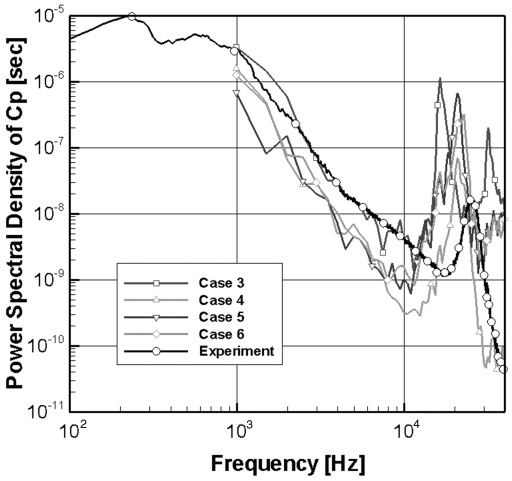

d) PSD at Point C

Fig. 7 Comparison of the power spectral density with the experiment.

improvements regarding 1) the level and frequency of the high-frequency narrowband peak, and 2) the level and distribution of the low-frequency broadband component, are observed.

C. Detail Observation of the Flowfield Inside the Slat Cove Region

Finally, detail observation of the flowfield inside the slat cove region will be performed in this section. Figure 8 shows the pressure fluctuation distribution on the $z/c = 0.025$ plane. The acoustic pulses, generated from the slat trailing edge, are clearly observed.

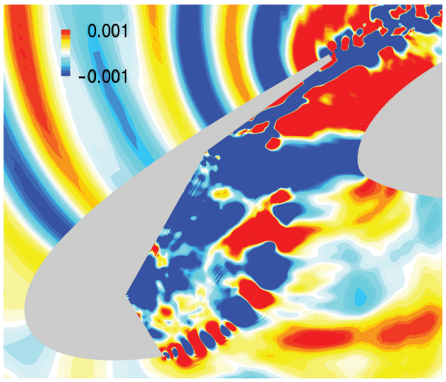

Fig. 8 Instantaneous pressure fluctuation field around the slat cove (case 5).

The wave length of the acoustic pulse generated from the trailing edge is approximately 0.27 c_{slat}, which corresponds to 20 kHz. The acoustic waves propagate around the slat cove region. Thus, the same peak at high frequency is observed at every point in Fig. 7. Figure 9 shows the pressure fluctuation on the slat surface. The left and right figures show the view of the upper and lower side of the slat, respectively. On the upper surface, the footprints of the acoustic waves generated from the slat trailing edge are visualized. They propagate upstream to the leading edge of the slat. Unfortunately, these waves seem to be restricted by the periodic boundary condition in the spanwise direction, because only the single cycle of pressure fluctuation can be seen in the spanwise direction. Although, the spanwise length of the computational model seems to be enough for the purpose of reproducing the breakup of the shear layer from the cusp and longitudinal vortex under the lower surface of the slat, further studies regarding this issue should be performed in the near future. On the lower side, the high-fluctuating region is observed where the shear layer impinges the lower surface of the slat. High- and low-pressure regions appear parallel to the mean flow direction.

To understand the unsteady property around the reattachment point of the shear layer, PSD is calculated. Figure 10 shows the PSD distribution calculated at points A to D for case 5. The results of points A to C are presented once again for reference. Point D is located at the reattachment point of the shear layer. The peak pressure fluctuations along the slat surface have been shown to occur near this location [11]. However, the pressure transducer could not be located at point D in the experiment, because the thickness near the slat

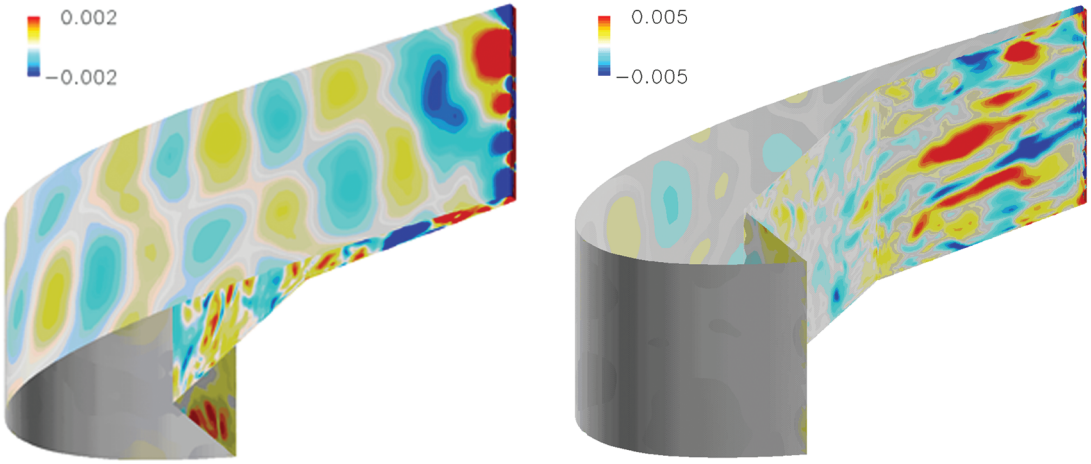

a) View from the upper side **b) View from the lower side**

Fig. 9 Instantaneous pressure fluctuations on the surface of the slat (case 5).

trailing edge is not enough. For the low-frequency broadband component, the level at point D is higher than that of points A to C by an order of magnitude. This indicates that point D is closer to the low-frequency broadband noise source compared with points A to C.

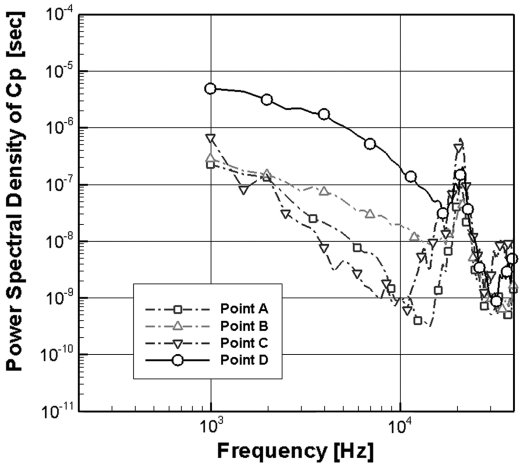

Fig. 10 PSD distribution for case 5.

Figure 11 shows the isosurface of the vorticity magnitude distribution for case 5. Figures 11a and 11b are colored by the spanwise and streamwise vorticity components, respectively. In Fig. 11a, the strong spanwise vorticity is observed starting from the slat cusp. As going downstream along the shear layer, the vorticity breaks up into a smaller size. Then, these vorticity impinge the lower surface of the slat. After the impingement, the negative spanwise vorticity (rotating in clockwise direction colored by blue) can be seen at the upstream side of the reattachment point. At the downstream side of the reattachment point, the streamwise vorticity becomes dominant as described in Fig. 11b. The change in the rotation axis of the dominant vorticity cannot be simulated by 2-D computations. However, by performing a 3-D zonal-LES/RANS computation, 3-D vortical structures inside the slat cove are simulated. These finding are consistent with the wind-tunnel experiment which has been performed by Takeda et al. [3] and also the numerical simulations by Choudhari et al. [11].

In Fig. 7b, the PSD level around 5 to 15 kHz of case 4 is lower compared with that of case 5. This frequency range corresponds to the higher part of the low-frequency broadband component, and this fluctuation is expected to be generated by relatively small-sized longitudinal vortices. When the third-order scheme is used in the simulation, the grid points required to resolve the vortices will increase. Thus, only longitudinal vortices with a relatively large

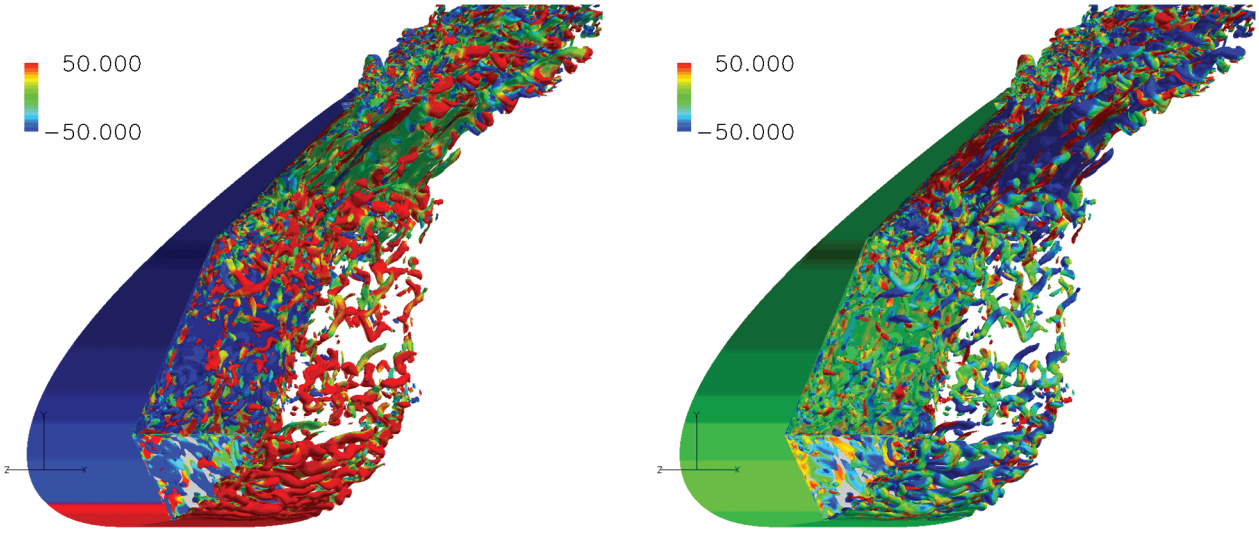

a) Vorticity magnitude isosurface colored by spanwise vorticity **b) Vorticity magnitude isosurface colored by streamwise vorticity**

Fig. 11 3-D Vorticity field in the slat cove region (case 5).

radius can be simulated by case 4. As a result, the higher part of the low-frequency broadband component is underestimated.

It is known that TKE, defined as

$$\mathrm{TKE} = \frac{1}{2}\sum_{i=1}^{3}\overline{u_i'^2}, \quad \text{where } u_i' = u_i - \overline{u_i} \tag{6}$$

has a close relation with the noise source (Ewert and Emunds [23]). However, it is known from the previous study [22] that the RANS model (such as the shear-stress-transport model) requires some kind of modification to obtain the TKE distribution which is consistent with the experimental data. Therefore, it is important to predict the TKE distribution correctly for the purpose of noise prediction. Figure 12 shows the cross-sectional TKE distribution. The high-TKE region appears from the slat cusp. First, the thickness of the high-TKE region increases as moving downstream along the shear layer. Then TKE decreases before impinging the lower surface of the slat. And after the impingement of the shear layer, the high-TKE region appears at the lower surface of the slat. Also, the high-TKE region caused by the vortex shedding at the trailing edge of the slat is simulated. The same TKE distribution pattern has been observed in the PIV measurements by Jenkins et al. [24] and the numerical simulation by Choudhari et al. [11].

The instantaneous 3-D distribution of the Powell noise source term is visualized in Fig. 13. The definition of the noise source is

$$q \equiv \rho_0 \mathrm{div}(\boldsymbol{\omega} \times \mathbf{u}) \tag{7}$$

This is based on Lighthill's acoustic analogy, and is valid for low-Mach number flow. The flow velocity inside the slat is small enough to satisfy this constraint. The red and blue isosurfaces indicate the positive and negative value of the noise source. The noise sources are observed at 1) the trailing edge where the vortex shedding occurs, 2) the lower surface of the slat near the trailing edge, and 3) the shear layer from the cusp. From the previous studies, the first location is known to be the cause of the high-frequency peak noise source of the slat. The noise sources are observed around the reattachment point of the shear layer and this supports the estimation that longitudinal vortices are the noise source for the low-frequency broadband component. By comparing the noise source's location with the TKE distribution described in Fig. 12, the close relation between the noise source and the high-TKE region can be observed.

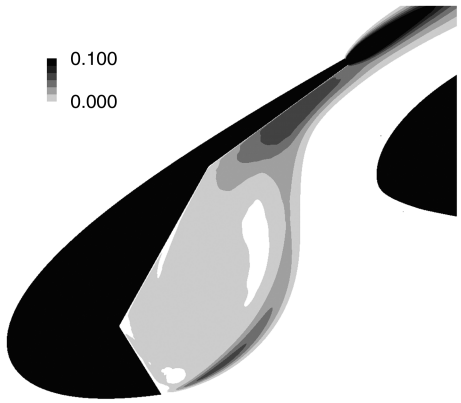

Fig. 12 Cross-sectional turbulent kinetic energy distribution (case 5).

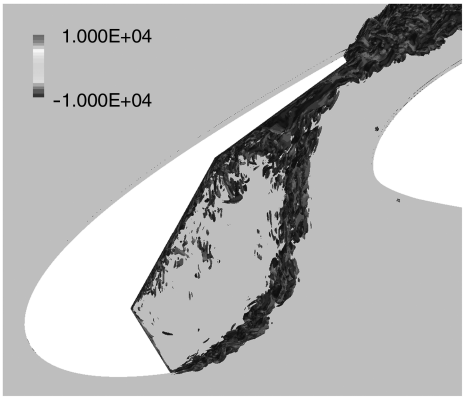

Fig. 13 Powell noise source around the slat cove (case 5).

IV. Conclusions

The 3-D unsteady flow inside the slat cove of a high-lift device is simulated numerically to investigate the cause of the slat noise. Because the Reynolds number of the flow is high and the geometry is complex, a zonal-LES/RANS hybrid method is used to reduce the overall computational cost. The power spectral density of C_p is compared with the experiment, and some issues regarding the grid resolution, order of numerical scheme, and number of subiterations for the implicit time integration are discussed. Two different types of fluctuations (high-frequency narrowband and low-frequency broadband) are observed. The computational result is consistent with the experiment and reinforces the findings of the previous investigations [2,3,11].

Using the computational data, the flow structures inside the slat cove region are visualized to understand the noise generation mechanism. As for the high-frequency peak, pressure pulse from the slat trailing edge is clearly visualized, and the peak frequency is consistent with the wave length observed in the instantaneous pressure fluctuation field. The present 3-D computation shows complicated 3-D vortical structures inside the slat cove. Change in the direction of dominant vorticity axis is observed where the shear layer impinges the lower surface of the slat. This phenomenon cannot be captured by 2-D computations and this fact indicates the importance of 3-D computation in the slat cove region. Since the highest level in PSD is observed at the lower surface of the slat near the trailing edge for the low-frequency broadband component, the longitudinal vortical structures are estimated as the cause of the low-frequency broadband noise. The instantaneous Powell noise source distribution and the time-averaged TKE distribution under the lower surface of the slat support this estimation.

Acknowledgments

We would like to thank K. Amemiya of the Foundation for the Promotion of Japanese Aerospace Technology, for performing some of the computations in this paper. Some of the computations are performed using the central machine of Numerical Simulator III system in JAXA.

References

[1] Hardin, J. C., "Airframe Self-Noise—Four Years of Research," NASA TM X-73908, 1976.

[2] Takeda, K., Ashcroft, G. B., Zhang, X., and Nelson, P. A., "Unsteady Aerodynamics of Slat Cove Flow in a High-Lift Device Configuration," AIAA Paper 2001-706, Jan. 2001.

[3] Takeda, K., Zhang, X., and Nelson, P. A., "Unsteady Aerodynamics and Aeroacoustics of a High-Lift Device Configuration," AIAA Paper 2002-0570, Jan. 2001.

[4] Pott-Pollenske, M., Alvarez-Gonzalez, J., and Dobrzynski, W., "Effect of Slat Gap/Overlap on Farfield Radiated Noise," AIAA Paper 2003-3228, May 2003.

[5] Kaepernick, K., Koop, L., and Ehrenfried, K., "Investigation of the Unsteady Flow Field Inside a Leading Edge Slat Cove," AIAA Paper 2005-2813, May 2005.

[6] Singer, B. A., Lockard, D. P., Brentner, K. S., Khorrami, M. R., Berkman, M. E., and Choudhari, M., "Computational Aeroacoustic Analysis of Slat Trailing-Edge Flow," AIAA Paper 99-1802, May 1999.

[7] Choudhari, M., Khorrami, M. R., Lockard, D. P., and Atkins, H. L., "Slat Cove Noise Modeling: A Posteriori Analysis of Unsteady RANS Simulations," AIAA Paper 2002-2468, June 2002.

[8] Khorrami, M. R., Choudhari, M. M., and Jenkins, L. N., "Characterization of Unsteady Flow Structures Near Leading-Edge Slat: Part 2, 2D Computations," AIAA Paper 2004-2802, May 2004.

[9] Terracol, M., Labourasse, E., Manoha, E., and Sagaut, P., "Simulation of the 3D Unsteady Flow in a Slat Cove for Noise Prediction," AIAA Paper 2003-3110, May 2003.

[10] Deck, S., "Zonal-Detached-Eddy Simulation of the Flow Around a High-Lift Configuration," *AIAA Journal*, Vol. 43, No. 11, Nov. 2005, pp. 2372–2384.
[11] Choudhari, M. M., and Khorrami, M. R., "Slat Cove Unsteadiness: Effect of 3D Flow Structures," AIAA Paper 2006-0211, Jan. 2006.
[12] Yamane, T., Yamamoto, K., Enomoto, S., Yamazaki, H., Takaki, R., and Iwamiya, T., "Development of a Common CFD Platform—UPACS," *Parallel Computational Fluid Dynamics—Proceedings of the Parallel CFD 2000 Conference*, Elsevier Science B.V., Trondheim, Norway, 2001, pp. 257–264.
[13] Takaki, R., Yamamoto, K., Yamane, T., Enomoto, S., and Mukai, J., "The Development of the UPACS CFD Environment," *High Performance Computing Proceedings of 5th International Sympoium, ISHPC 2003*, edited by A. Veidenbaum, K. Joe, H. Amano, and H. Aiso, Springer, New York, 2003, pp. 307–319.
[14] Murayama, M., Yamamoto, K., and Kobayashi, K., "Validation of Computations Around High-Lift Configurations by Structured- and Unstructured-Mesh," *Journal of Aircraft*, Vol. 43, No. 2, March–April 2006, pp. 395–406.
[15] Ito, T., Yokokawa, Y., Ura, H., Kato, H., Mitsuo, K., and Yamamoto, K., "High-Lift Device Testing in JAXA 6.5M X 5.5M Low-Speed Wind Tunnel," AIAA Paper 2006-3643, June 2006.
[16] Yokokawa, Y., Murayama, M., Ito, T., and Yamamoto, K., "Experiment and CFD of a High-Lift Configuration Civil Transport Aircraft Model," AIAA Paper 2006-3452, June 2006.
[17] Smagorinsky, J., "General Circulation Experiments with the Primitive Equations," *Monthly Weather Review*, Vol. 91, No. 3, 1963, pp. 99–164.
doi:10.1175/1520-0493(1963)091<0099:GCEWTP>2.3.CO;2
[18] Spalart, P. R., and Allmaras, S. R., "A One-Equation Turbulence Model for Aerodynamic Flows," AIAA Paper 92-0439, Jan. 1992.
[19] Shima, E., "A Simple Implicit Scheme for Structured/Unstructured CFD," *Proceedings of 29th Fluid Dynamics Symposium, Hokkaido, Japan*, The Japan Society for Aeronautical and Space Sciences, Tokyo, 1997, pp. 325–328 (in Japanese).
[20] Kobayashi, M. H., "On a Class of Pade Finite Volume Methods," *Journal of Computational Physics*, Vol. 156, No. 1, Nov. 1999, pp. 137–180.
doi:10.1006/jcph.1999.6376
[21] Gaitonde, D. V., and Visbal, M. R., "Pade-±-Type Higher-Order Boundary Filters for the Navier-Stokes Equations," *AIAA Journal*, Vol. 38, No. 11, 2000, pp. 2103–2112.
[22] Visbal, M. R., and Gaitonde, D. V., "Very High-Order Spatially Implicit Schemes for Computational Acoustics on Curvilinear Meshes," *Journal of Computational Acoustics*, Vol. 9, No. 4, Dec. 2001, pp. 1259–1286.
[23] Ewert, R., and Emunds, R., "CAA Slat Noise Studies Applying Stochastic Sound Sources Based On Solenoidal Digital Filters," AIAA Paper 2005-2862, May 2005.
[24] Jenkins, L. N., Khorrami, M. R., and Choudhari, M., "Characterization of Unsteady Flow Structures Near Leading-Edge Slat: Part 1, PIV Measurements," AIAA Paper 2004-2801, May 2004.

R. So
Associate Editor